

Average Torque Separation in Permanent Magnet Synchronous Machines Using Frozen Permeability

W. Q. Chu and Z. Q. Zhu, *Fellow, IEEE*

Department of Electronic and Electrical Engineering, University of Sheffield, Sheffield S1 3JD, U.K.

This paper investigates the average torque separation in permanent magnet (PM) synchronous machines. In order to accurately separate the PM and armature fields, and, hence, the torque components accounting for the magnetic saturation and crosscoupling, the frozen permeability (FP) method is often employed, while the torque can be calculated by different methods, such as Maxwell stress tensor and virtual work principle. Although these two methods result in identical torques in normal finite element (FE) analyses when appropriate FE meshes are used, the average torques calculated by these two methods are found to be different when the FP method is employed due to the influence of equivalent rotational magnetic saliency in the stator, which causes a part of PM torque being improperly attributed to the reluctance torque when Maxwell stress tensor method is employed. However, by using the virtual work principle, this is eliminated, and, hence, the average torque components can still be appropriately separated and analyzed.

Index Terms—Average torque separation, crosscoupling, frozen permeability (FP), magnetic saturation, permanent magnet (PM) machines.

I. INTRODUCTION

DUE to high torque density and efficiency, permanent magnet (PM) machines are popular in various applications, such as electrical vehicles, power generations, and aerospace and industrial applications [1]–[9].

It is well known that the average torque in PM machines is contributed by two components: the PM and reluctance torques. The PM torque is due to the interaction between the PM and armature fields, while the reluctance torque is due to the interaction between the armature field and the rotor magnetic saliency. The separation of average torque into its PM and reluctance components will provide valuable insights for PM machine design and optimization.

For the torque calculation, the Maxwell stress tensor and virtual work principle are two most well-known and widely used methods [10]–[18]. Based on the Maxwell stress tensor method, the torque is calculated directly from the radial and tangential flux density components. Based on the virtual work principle, the torque may be calculated from the flux linkages. It is also well known that the torques calculated by these two methods should be identical, at least theoretically, in normal finite element (FE) analyses [10]–[17] although they may be influenced by the FE mesh discretization, etc.

However, for the average torque separation, the flux density or flux linkage components due to on-load PM or armature field are required. Three methods have been reported in the existing literature for the average torque separation [19]–[22]: 1) the constant PM flux linkage model; 2) the partial-coupling model [19], in which the PM flux linkage varies with the q -axis current only; and 3) the frozen permeability (FP) FE method. Since the

PM and armature fields influence each other and change with the magnetic saturation and crosscoupling, both the constant PM flux linkage model and the partial-coupling model may result in significant inaccuracy. Hence, the FP method is often employed [20]–[30], in order to accurately separate the PM and armature fields and hence the torque components accounting for the magnetic saturation and crosscoupling.

Based on the FP method, there are two ways of average torque separation: 1) based on the Maxwell stress tensor method, the reluctance torque is computed with the on-load armature field only and the PM torque is then calculated from the difference between the total torque and reluctance torque [16]; and 2) based on the virtual work method, the PM and reluctance torque components are calculated from the flux linkages contributed by the on-load PM or armature field only [20]–[23]. Since the torques calculated by the Maxwell stress tensor method and virtual work principle are identical in normal FE analyses, both methods are assumed to be accurate and widely employed for the torque separation in the literature. However, none of them has been validated when the FP method is employed. Therefore, in this paper, for the first time, the average torque components separated by the Maxwell stress tensor and virtual work principle are compared and examined when the FP method is employed. It is found that the average torque components predicted by these two methods are different. When the FP method is employed, the average torque separation can be performed appropriately by virtual work principle while the Maxwell stress tensor cannot.

The investigation is carried out on an inset PM prototype machine, which is described in Section II. The FP method is illustrated and the on-load field components are separated and analyzed in Section III. The Maxwell stress tensor method and the virtual work principle are first examined and compared in normal FE analyses for the total torque calculation in Section IV and further investigated in Section V for the average torque separation when the FP method is employed. The cause for the torque discrepancy is explained in Section V as well. Finally, the variation of average torque components is obtained and analyzed in Section VI.

Manuscript received June 22, 2012; revised August 27, 2012; accepted October 09, 2012. Date of publication October 16, 2012; date of current version February 20, 2013. Corresponding author: Z. Q. Zhu (e-mail: z.q.zhu@sheffield.ac.uk).

Color versions of one or more of the figures in this paper are available online at <http://ieeexplore.ieee.org>.

Digital Object Identifier 10.1109/TMAG.2012.2225068

TABLE I
MAIN PARAMETERS

Parameters	value	Parameters	value
Outer diameter	106mm	Rated current (peak)	4A
Stator inner diameter	62mm	Number of turns per phase	152
Airgap length	0.75 mm	Magnet thickness	18.2mm
Axial length	30mm	Remanence	1.17T
Slot number	18	Coercive force	-891 kA/m
Pole number	6		

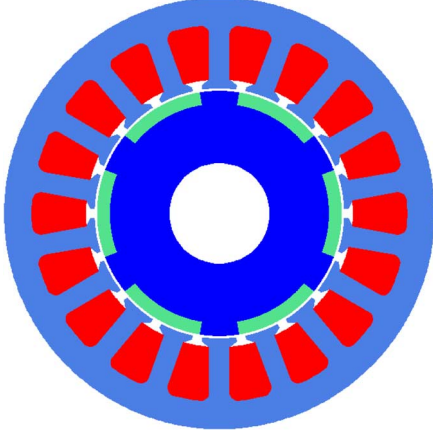


Fig. 1. Cross section of the inset PM machine.

II. PROTOTYPE MACHINE

In order to reveal the influence of magnetic saturation and crosscoupling, as well as the variation of PM and reluctance torque components, the investigations are carried out on an inset PM prototype machine, whose cross section and parameters are given in Table I and Fig. 1. All the simulations are carried out by the commercial FE software OPERA. The phase current is ideal sinusoidal and the current phase advance angle β is referred to the positive q -axis. When $0^\circ < \beta < 90^\circ$, the q -axis current is positive and the d -axis current is negative.

III. FROZEN PERMEABILITY METHOD

A. Principle and Procedure

The FP method has been widely used to investigate the issues related with magnetic saturation and crosscoupling [20]–[30]. Its principle is illustrated and compared with the conventional method in Fig. 2.

Without using the FP method, with the PM excitation (H_{PM}) only, i.e., open circuit, the resultant flux density is B_{PM} (point B). With the armature excitation (H_i) only, the resultant flux density is B_i (point C). When it is on load (point A), the PM machine is excited by both PM and current, i.e., $H_{all} = H_{PM} + H_i$. However, the resultant flux density B_{all} is lower than $B_{PM} + B_i$. The on-load PM and armature field components cannot be decomposed.

In the FP method, the on-load permeability μ_{all} is first obtained and stored by solving the on-load model (point A). Then, two linear analyses, represented by points D and E, can be solved further based on the frozen μ_{all} : with either the PM or armature excitation only to obtain $B(FP, PM)$ or

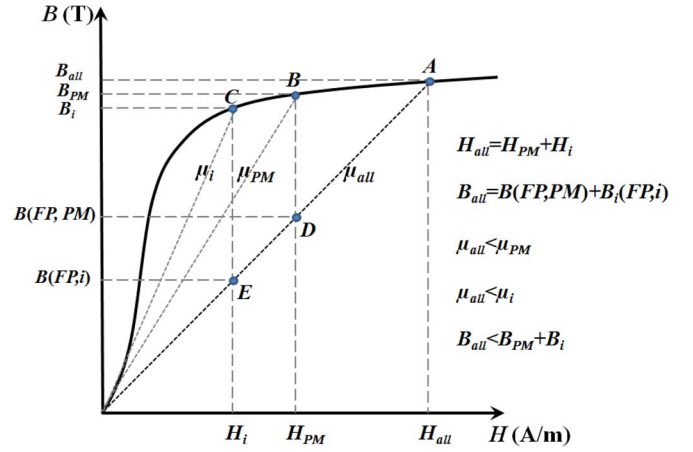


Fig. 2. Principle of the frozen permeability method.

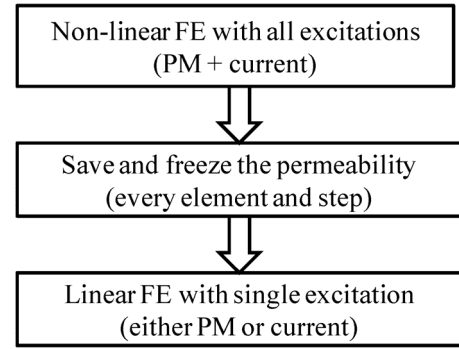


Fig. 3. Procedure of the frozen permeability method.

$B(FP, i)$, respectively. Since the nonlinear problem has been transformed into the linear one by freezing the permeability as μ_{all} , $B_{all} = B(FP, PM) + B(FP, i)$. Therefore, the on-load PM and armature field components are decomposed. Furthermore, since μ_{all} varies according to the operation point, the influence of magnetic saturation and crosscoupling is also included.

Based on the principle of the FP method, the procedure in the FE computation is summarized in Fig. 3. First, the nonlinear FE model with all excitations (PM and current), referred to as the whole model, is solved. Second, the permeability of the whole model, referred to as on-load permeability, in each element and each step, is saved and frozen. Finally, the on-load PM or armature field component is obtained by solving the linear FE model based on the on-load permeability, with either PM or armature excitation only, respectively.

B. Field Distributions

By using the FP method, the on-load PM and armature field components can be obtained. For example, the on-load field distributions when the peak phase current I_a is 4 A, $\beta = 0^\circ$, and rotor position θ is 0° (electrical), are shown in Fig. 4.

It can be seen that the on-load field and permeability distributions are neither symmetrical with the d -axis nor with the q -axis due to the influence of armature field [Fig. 4(a) and (b)]. Therefore, the on-load PM field [Fig. 4(c)] is asymmetric with the d -axis and has q -axis flux linkage, although the PM excitation

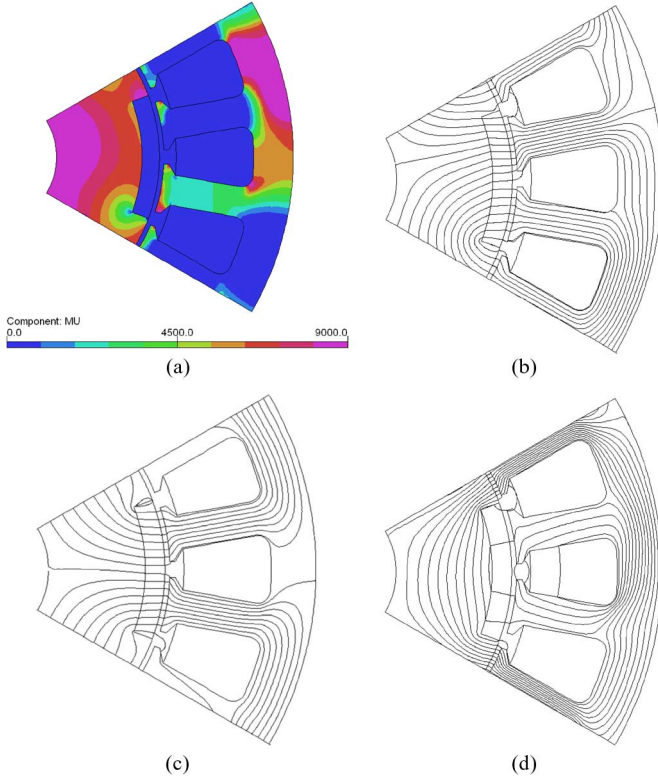


Fig. 4. On-load field distributions when $I_a = 4$ A, $\beta = 0^\circ$, and $\theta = 0^\circ$. (a) On-load permeability; (b) whole field (PM and current); (c) on-load PM field (FP); and (d) on-load armature field (FP).

is aligned with the d -axis. It is also true for the on-load armature field. Although only q -axis current is applied, the on-load armature field [Fig. 4(d)] is asymmetric with the q -axis and has d -axis flux linkage.

For further illustration of on-load field decomposition, the radial and tangential flux density components along the middle of air gap in Fig. 4 are obtained and shown in Fig. 5. It can be seen that, for each point, the flux densities in the whole model (PM and current) is the same as the mathematical summation of the two flux density components, with either the on-load PM or armature field only, respectively. This is also true for any other rotor position and load condition, as will be shown later.

C. Flux Linkage Results

Based on the foregoing investigation, the complete flux linkage model should be given by [20], [21]

$$\psi_d = \psi_d(\text{PM}) + \psi_d(i) = \psi_d(\text{PM}) + L_{dd}I_d + L_{dq}I_q \quad (1)$$

$$\psi_q = \psi_q(\text{PM}) + \psi_q(i) = \psi_q(\text{PM}) + L_{dq}I_d + L_{qq}I_q \quad (2)$$

where ψ_d and ψ_q are total d - and q -axis flux linkages, respectively. $\psi_d(\text{PM})$ and $\psi_q(\text{PM})$ are the d - and q -axis flux linkages due to on-load PM field, respectively. $\psi_d(i)$ and $\psi_q(i)$ are d - and q -axis flux linkages due to on-load armature field, respectively. I_d and I_q are d - and q -axis currents, respectively. L_{dd} , L_{qq} , and L_{dq} are d - and q -axis self and mutual inductances, respectively.

The variation of flux linkage components with rotor position is shown in Fig. 6. It can be seen more clearly that not only

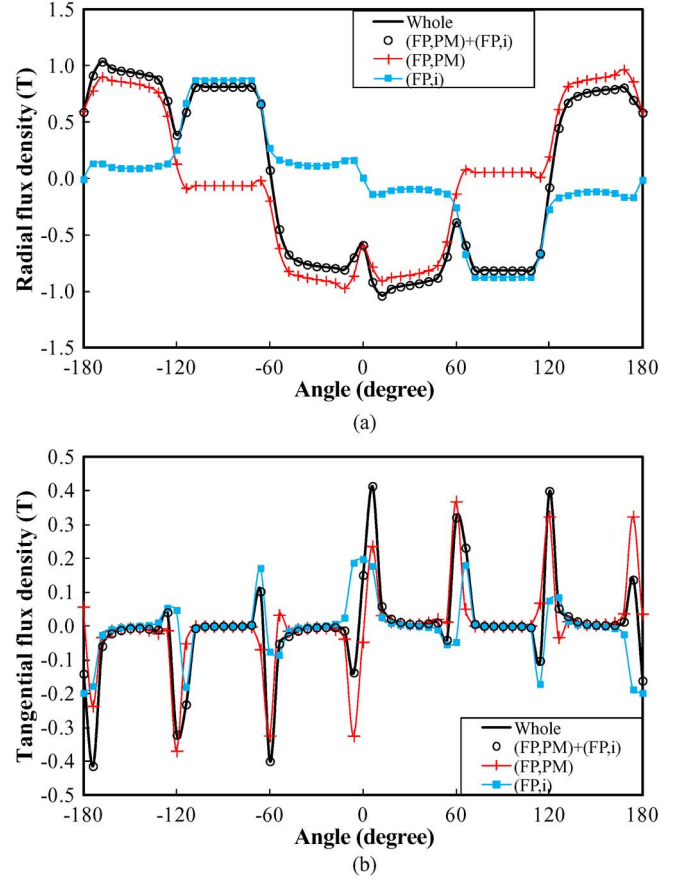


Fig. 5. Flux density components in middle of air gap when $I_a = 4$ A, $\beta = 0^\circ$, and $\theta = 0^\circ$. (a) Radial flux density components; and (b) tangential flux density components.

the instantaneous $\psi_q(\text{PM})$ but also its average is not zero. The average of $\psi_d(i)$ is also not zero, although only q -axis current is applied. These are due to the influence of crosscoupling, which has been illustrated in Fig. 4.

The variation of average flux linkages and inductances with β is shown in Fig. 7. The influence of magnetic saturation is represented by $\psi_d(\text{PM})$, L_{dd} , and L_{qq} . When $\beta = -90^\circ$, I_d is positive maximum. The d -axis magnetic saturation is the heaviest due to maximum flux enhancing. Hence, $\psi_d(\text{PM})$ and L_{dd} are minimum. When $\beta = 0^\circ$, I_d is zero and I_q is maximum. The magnetic saturation is modest along the d -axis but the heaviest along the q -axis. Therefore, $\psi_d(\text{PM})$ and L_{dd} are higher while L_{qq} is the lowest. When $\beta = 90^\circ$, the I_d is negative maximum and the magnetic saturation along the d -axis is the lowest due to maximum flux weakening. Therefore, $\psi_d(\text{PM})$ and L_{dd} are maximum. The influence of crosscoupling is represented by $\psi_q(\text{PM})$ and L_{dq} . The crosscoupling is zero and hence $\psi_q(\text{PM})$ and L_{dq} are zero when $\beta = \pm 90^\circ$ since I_q is zero. Although I_q is maximum when $\beta = 0^\circ$, the crosscoupling is the heaviest and hence $\psi_q(\text{PM})$ and L_{dq} reach the peak at $\beta = -30^\circ$ since it is aggravated by the magnetic saturation. Therefore, the on-load PM and armature field components can be decomposed by the FP method accounting for the influence of saturation and crosscoupling. Hence, it is possible to separate the total torque into its PM and reluctance components based on the FP method.

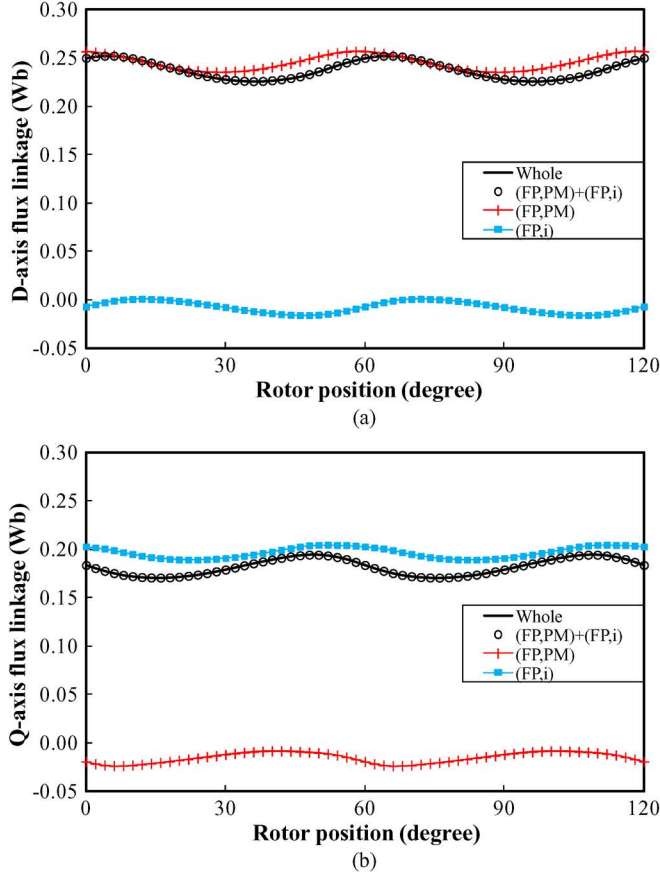


Fig. 6. Variation of flux linkages with rotor position when $I_a = 4$ A and $\beta = 0^\circ$: (a) d -axis flux linkages; and (b) q -axis flux linkages.

IV. TORQUE CALCULATION METHODS

For the torque calculation, the Maxwell stress tensor and virtual work principle are two most well-known and widely used methods [10]–[18]. Based on the Maxwell stress tensor method, the torque is calculated from an integral directly from the flux density components

$$T_{mw} = \frac{L_{ef}}{\mu_0} \int_0^{2\pi} r^2 B_n B_t d\theta_m \quad (3)$$

where μ_0 is the permeability of free space, L_{ef} is the effective axial length, r is the radius of integration path, and B_n and B_t are the normal and tangential flux density components, respectively.

Based on the virtual work principle, the torque is obtained from the energy conservation law. For an open conservative lossless system, the torque is given as [15], [16]

$$T_{vir} = \frac{\partial W'_m}{\partial \theta_m} = \frac{\partial W_{in}}{\partial \theta_m} - \frac{\partial W_m}{\partial \theta_m} = T_{in} - \frac{\partial W_m}{\partial \theta_m} \quad (4)$$

where W'_m is the magnetic co-energy, W_{in} and T_{in} are the input energy and corresponding torque, W_m is the stored magnetic energy in the machine, and θ_m is the rotor position in mechanical angle.

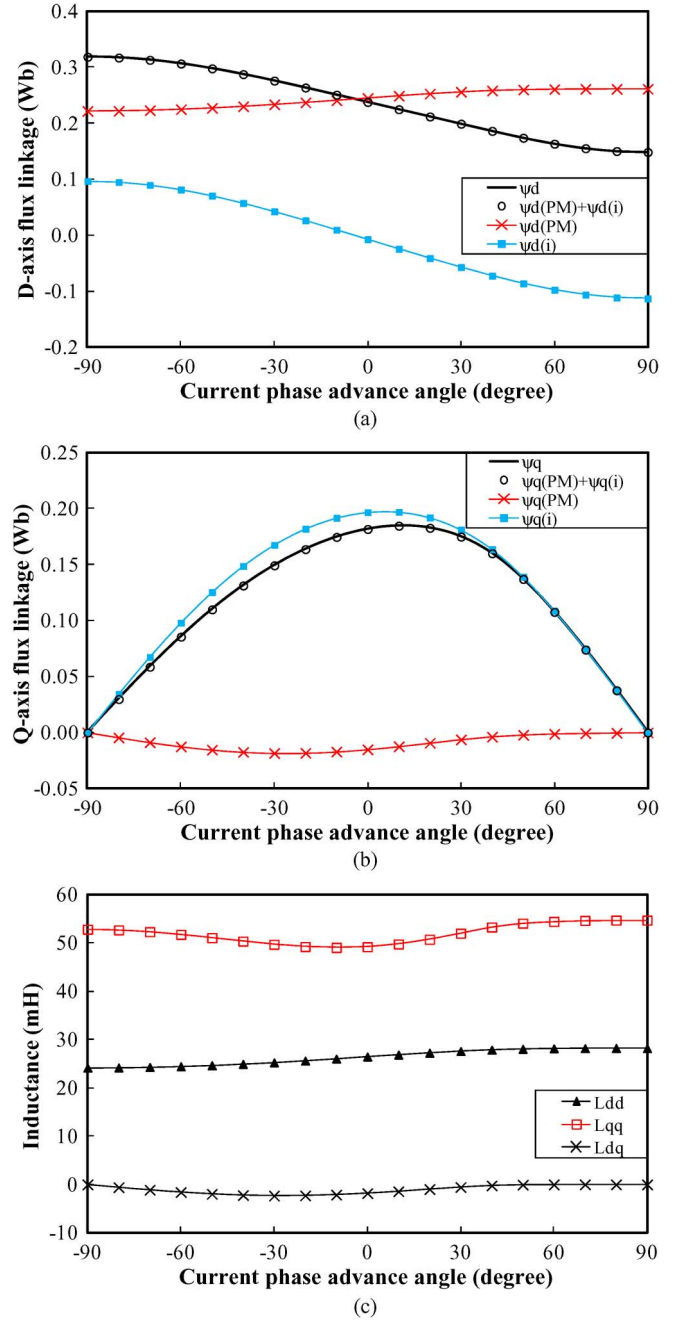


Fig. 7. Variation of average flux linkages and inductance with β when $I_a = 4$ A: (a) d -axis flux linkages; (b) q -axis flux linkages; and (c) inductances.

The calculation of W_m is detailed in the Appendix and for electrical machines, T_{in} can be calculated as [31]–[34]

$$T_{in} = \frac{3}{2}p \left(I_d \frac{d\psi_d}{d\theta} + I_q \frac{d\psi_q}{d\theta} + \psi_d I_q - \psi_q I_d \right). \quad (5)$$

In this paper, the torque obtained by OPERA is based on the Maxwell stress tensor method and the torque based on virtual work principle is calculated through flux linkage results, as shown in (4) and (5). It is well known that these two methods are identical for torque calculation in normal FE simulations

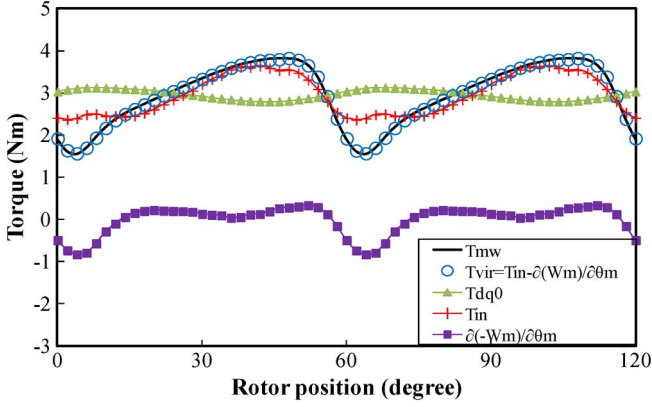


Fig. 8. Torque waveforms when $I_a = 4.0$ A and $\beta = -30^\circ$.

[10]–[17], although attention should be paid to the mesh discretization. For example, the instantaneous torque waveforms based on the Maxwell stress tensor method and virtual work principle are obtained and shown in Fig. 8. It can be seen that the torque results based on these two methods are the same, as expected, which also indicates that the mesh discretization is appropriate and, hence, its influence is negligible.

Furthermore, for (4) and (5), it can be noticed that $\partial W_m / \partial \theta_m$, $\psi_d / d\theta$, and $\psi_q / d\theta$ have no contribution to the average torque, since the magnetic field repeats every cycle. Hence, for the average torque, it can also be calculated by the classical $dq0$ model as

$$T_{dq0} = 1.5p(\psi_d I_q - \psi_q I_d). \quad (6)$$

Without the derivative operation and calculation of magnetic energy, (6) is much simpler and more widely used than (4) and (5) for the average torque calculation. It also has been validated in various machines on the average torque calculation even when the machine is heavily saturated or the winding layout is far from sinusoidal [17], [35]–[37]. The drawback of (6) is that it cannot be used for the instantaneous torque and torque ripple computation, as shown in Fig. 8. However, it does not influence the average torque separation.

V. AVERAGE TORQUE SEPARATION BASED ON FROZEN PERMEABILITY METHOD

As stated foregoing, in order to separate the on-load PM and armature fields and, hence, the average torque components accurately, the FP method are often employed. The same as normal simulations, when the FP is applied, two torque results can be obtained from every FE solution, based on the Maxwell stress tensor method or virtual work principle, respectively. Therefore, there are two possible ways of the average torque separation, which are summarized in Fig. 9 and Table II.

The torque separation in [15] is based on the Maxwell stress tensor method. The reluctance torque is computed with the on-load armature field only by (7). The PM torque is then calculated as the difference between the total torque and the

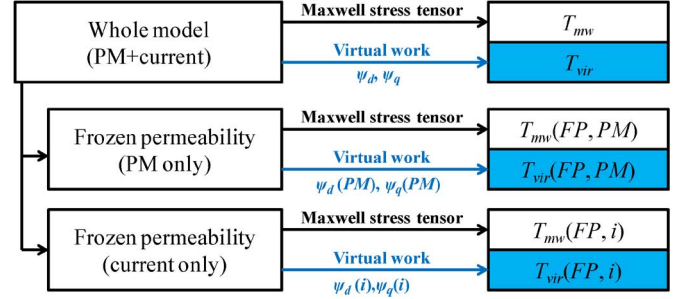


Fig. 9. Relationships between FE solutions and torque results.

TABLE II
ON-LOAD AVERAGE TORQUE SEPARATION AND COMPONENTS

	Maxwell stress tensor	Virtual work
Total torque	T_{mw}	T_{vir}
Reluctance torque	$T_{mw}(FP, i)$	$T_{vir}(FP, i)$
PM torque	$T_{mw} - T_{mw}(FP, i)$	$T_{vir}(PM)$ or $T_{vir} - T_{vir}(FP, i)$
On-load PM field	$T_{mw}(FP, PM)$	$T_{vir}(FP, PM)$

reluctance torque by (8). The output torque with on-load PM field only is the on-load cogging torque as given in (9)

$$T_{mw}(\text{rel}) = T_{mw}(FP, i) = \frac{L_{ef}}{\mu_0} \int_0^{2\pi} r^2 B_n(i) B_t(i) d\theta_m \quad (7)$$

$$T_{mw}(PM) = T_{mw} - T_{mw}(FP, i) \quad (8)$$

$$T_{mw}(FP, PM) = \frac{L_{ef}}{\mu_0} \int_0^{2\pi} r^2 B_n(PM) B_t(PM) d\theta_m \quad (9)$$

where $B_n(i)$ and $B_t(i)$ are the normal and tangential flux density components due to the on-load armature field only, and $B_n(PM)$ and $B_t(PM)$ are the normal and tangential flux density components due to the on-load PM field only.

The average torque separations in [20]–[23] are based on the virtual work principle. Since only the average torque is concerned, the torque components are estimated by

$$T_{vir}(\text{rel}) = T_{vir}(FP, i) = 1.5p[\psi_d(i)I_q - \psi_q(i)I_d] \quad (10)$$

$$T_{vir}(PM) = 1.5p[\psi_d(PM)I_q - \psi_q(PM)I_d] = T_{vir} - T_{vir}(FP, i) \quad (11)$$

$$T_{vir}(FP, PM) = 0 \quad (12)$$

based on the classical $dq0$ model. In order to identify the calculation method and the related torque components, (10)–(12) are labeled as $T_{vir}(\text{rel})$, $T_{vir}(PM)$, and $T_{vir}(FP, PM)$, respectively.

However, it should be noted that (10)–(12) are different from the actual reluctance torque, the PM torque, and the on-load cogging torque, respectively, since the torque ripples are inaccurate. Therefore, (10)–(12) are only suitable for the average torque evaluation but not for the torque waveform and torque ripples.

By way of example, when with the on-load PM field only, the torque predicted by (12) is always zero. The average torque

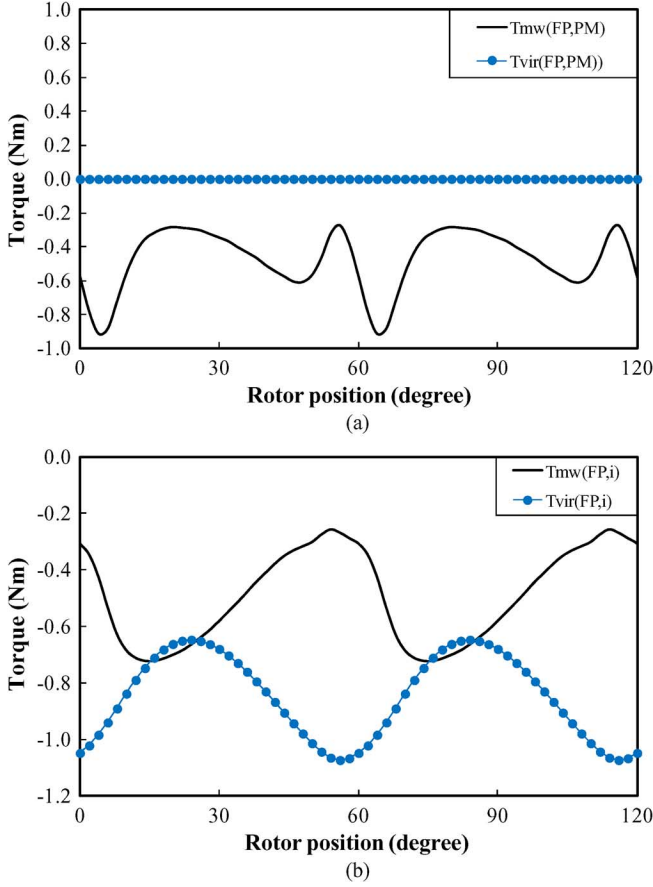


Fig. 10. Torque results based on Maxwell stress tensor and virtual work principle when $I_a = 4.0$ A and $\beta = -30^\circ$. (a) Related torque with on-load PM field (FP) only. (b) Related torque with on-load armature field (FP) only.

is zero, since the phase current and input power are zero. The predicted torque ripple is zero due to that the variation of stored magnetic energy, which results in the on-load cogging torque, is excluded in (12).

However, neither the Maxwell stress tensor method nor the virtual work principle has been verified in literature when the FP is employed. Therefore, it is important and necessary to examine and compare these two ways of torque separation when the FP is employed.

As can be seen from Figs. 10 and 11, when the FP method is applied, the average torques calculated by the Maxwell stress tensor or virtual work methods are different. With the on-load PM field only, the average of $T_{mw}(FP, PM)$ based on the Maxwell stress tensor method is always lower than the average of $T_{vir}(FP, PM)$, which is zero and based on the virtual work principle. With the on-load armature field only, the average of $T_{mw}(FP, i)$ based on the Maxwell stress tensor method is always higher than the average of $T_{vir}(FP, i)$ based on the virtual work principle. Hence, it is important to find out what causes the discrepancy of average torque and which one performs the average torque separation properly. For these purposes, the torque results with on-load PM field only are utilized due to its unique features: the phase current is zero and the torque is manifested by the PM only, which is similar with the open circuit one. Therefore, the average of resultant

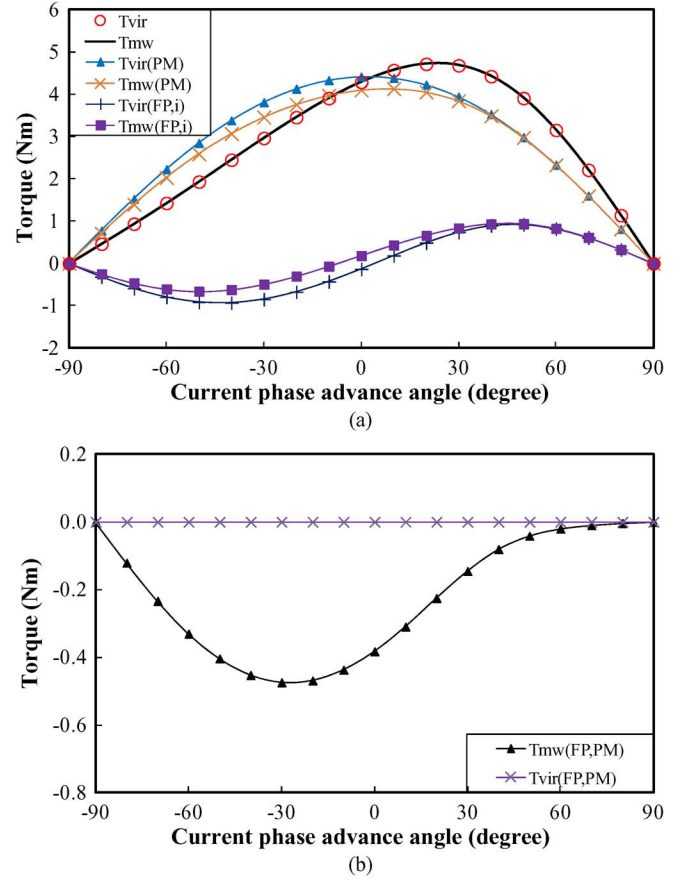


Fig. 11. Variation of average torque and separated torque components with current phase advance angle based on Maxwell stress tensor and virtual work principle. (a) Average torque results. (b) Related torque with on-load PM field (FP) only.

torque, i.e., on-load cogging torque, must be zero. Hence, it can be concluded that the Maxwell stress tensor method cannot provide the torque calculation properly when the FP method is applied since its calculated average torque is not zero with the on-load PM field excitation only.

However, it is also important to find out why the average of $T_{mw}(FP, PM)$ is nonzero. In order to aid the analyses, the results with the on-load PM field only are compared with the open-circuit one in Figs. 12–14. In Figs. 12 and 13, the permeability distributions at two representative rotor positions, i.e., $\theta = 0^\circ$ and $\theta = 30^\circ$, are illustrated, respectively. When it is on open circuit, the torque is zero at both rotor positions due to the symmetrical permeability distribution, as shown in Figs. 12 and 14. However, the on-load permeability distribution is asymmetric with the PM due to the influence of armature field, both in the rotor and stator, as shown in Fig. 13. In other words, there is an equivalent magnetic saliency in the stator as well. Therefore, when the on-load PM field is applied, the nonzero torque is produced due to the interaction between PM and equivalent rotational magnetic saliency in the stator. It can be seen from Fig. 13, for both rotor positions, that there will be a negative torque on the rotor. Furthermore, since the armature field rotates synchronously with the rotor, the equivalent magnetic saliency in the stator rotates synchronously with the rotor as well. For this prototype, the PM excitation is always in advance of the high

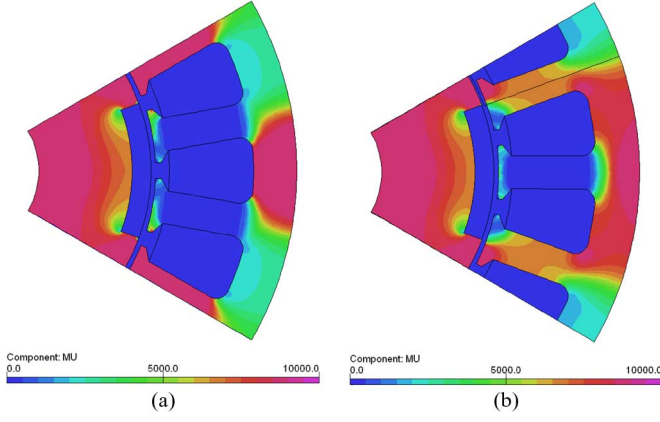


Fig. 12. Permeability distributions on open circuit: (a) $\theta = 0^\circ$; and (b) $\theta = 30^\circ$.

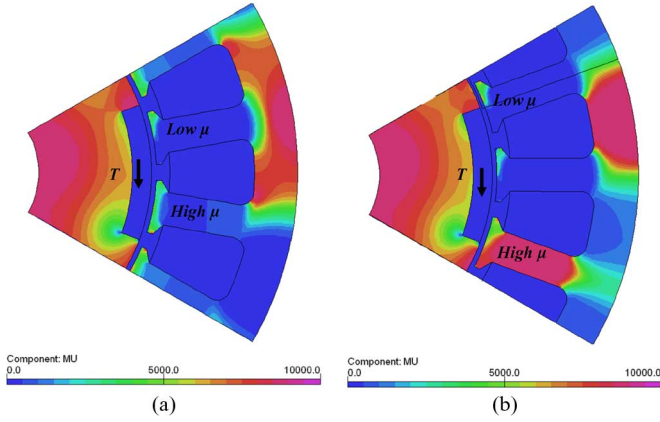


Fig. 13. Permeability distributions on load when $I_a = 4.0$ A and $\beta = -30^\circ$: (a) $\theta = 0^\circ$; and (b) $\theta = 30^\circ$.

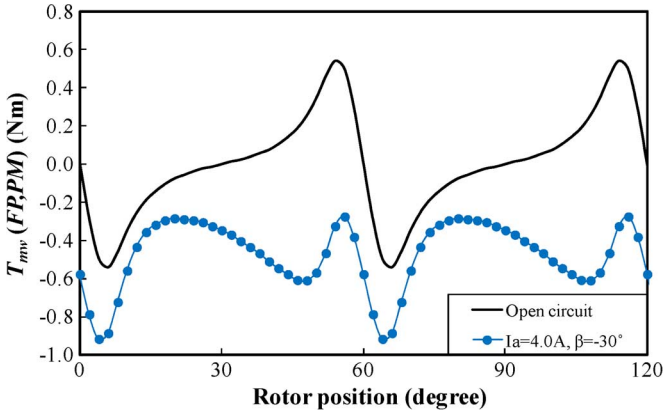


Fig. 14. Torque waveforms based on the Maxwell stress tensor.

permeance region in the stator. Therefore, the average torque per cycle with on-load PM field only is negative, as shown in Fig. 14. The mechanism of “produced” torque is the same as the reluctance torque.

The nonzero average torque of $T_{mw}(\text{FP, PM})$ can also be explained based on the on-load PM flux linkage results. As can be seen from Fig. 15, on open circuit, the average of $\psi_q(\text{PM})$ per cycle is zero, due to the fact that there is no equivalent rotational magnetic saliency in the stator. However, when it is on load, the average $\psi_q(\text{PM})$ per cycle is negative due to the equivalent rotational stator saliency. By reacting with positive

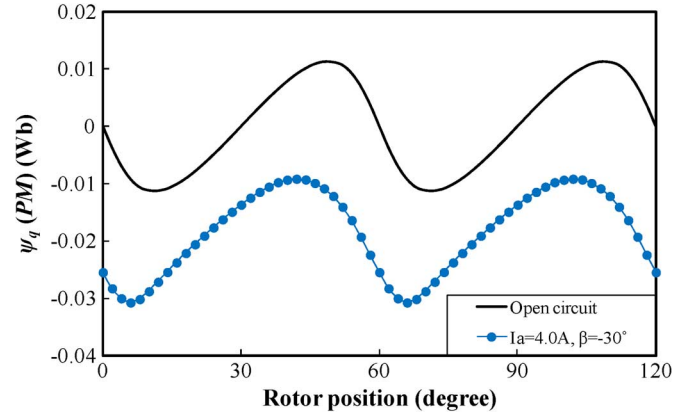


Fig. 15. Flux linkages results.

$\psi_d(\text{PM})$, the negative average $\psi_q(\text{PM})$ results in the negative average of $T_{mw}(\text{FP, PM})$, as shown Fig. 11(b).

Alternatively, it may be explained that when the on-load armature field is applied, this equivalent rotational magnetic saliency will react with the armature field and produce an extra torque component. Since the high permeance region in the stator is always in advance of the armature excitation in this prototype machine, $T_{mw}(\text{FP, } i)$ is always higher than $T_{vir}(\text{FP, } i)$, as shown in Fig. 11(a). Similarly, when it is a generator, it can be predicted that $T_{mw}(\text{FP, PM})$ will be higher than $T_{vir}(\text{FP, PM})$, which is zero, and $T_{mw}(\text{FP, } i)$ will be lower than $T_{vir}(\text{FP, } i)$. According to Fig. 11, it also can be seen that the influence of equivalent rotational magnetic saliency in the stator changes similarly with the crosscoupling: it reaches the peak when $\beta = -30^\circ$ and vanishes when $\beta = \pm 90^\circ$.

Since the on-load permeability distribution, and, hence, the equivalent rotational magnetic saliency in the stator, is a result of the interaction between PM and armature fields, the relevant torque, whose average torque is nonzero, should be a part of the PM torque. However, when using the Maxwell stress tensor method for the torque calculation with the FP method, the relevant torque due to the equivalent rotational magnetic saliency in the stator is included in $T_{mw}(\text{FP, PM})$ and $T_{mw}(\text{FP, } i)$. It is a fundamental limit for the torque calculation based on the combination of the Maxwell stress tensor and the FP method. Therefore, neither $T_{mw}(\text{FP, } i)$ is the reluctance torque nor $T_{mw}(\text{FP, PM})$ is the on-load cogging torque.

By using the virtual work principle, the improper torque attribution is eliminated, and, hence, the average torque calculations and separations are still performed properly, as given in (10)–(12).

VI. VARIATION OF TORQUE COMPONENTS

Based on the magnetic model in (1) and (2), the on-load torque is further divided as follows:

$$T_{\text{PM}} = T_{\text{PM}}(d) + T_{\text{PM}}(q) \quad (13)$$

$$T_{\text{PM}}(d) = 1.5p\psi_q(\text{PM})I_q \quad (14)$$

$$T_{\text{PM}}(q) = -1.5p\psi_q(\text{PM})I_d \quad (15)$$

$$T_r = T_r(d - q) + T_r(dq) \quad (16)$$

$$T_r(d - q) = 1.5p(L_{dd} - L_{qq})I_dI_q \quad (17)$$

$$T_r(dq) = 1.5pL_{dq}(I_q^2 - I_d^2) \quad (18)$$

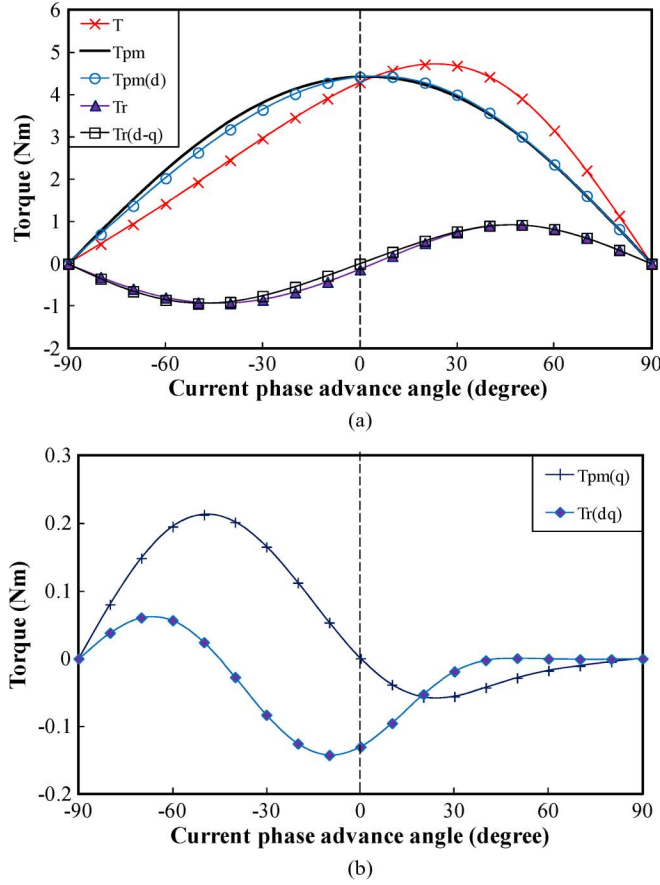


Fig. 16. Variation of average torque components. (a) Main torque components. (b) Torque components due to crosscoupling.

where T_{PM} , $T_{PM}(d)$, and $T_{PM}(q)$ are the PM torque and its components due to $\psi_d(\text{PM})$ and $\psi_q(\text{PM})$, respectively; and T_r , $T_r(d-q)$, and $T_r(dq)$ are the reluctance torque and its components due to the self-inductances and mutual inductance, respectively.

The variation of average torque components with the current phase advance angle is shown in Fig. 16. Together with the flux linkages and inductances in Fig. 7, the variation can be explained as follows.

$T_{PM}(d)$ and $T_r(d-q)$ are influenced by the magnetic saturation. Since $\psi_d(\text{PM})$ and L_{dd} increase with β , the positive β will result in higher $T_{PM}(d)$ and lower $|T_r(d-q)|$ than the negative β , for example, $T_{PM}(d)$ at $\beta = 30^\circ$ is higher than $T_m(d)$ at $\beta = -30^\circ$. $T_{PM}(d)$ reaches the peak at $\beta = 10^\circ$.

$T_{PM}(q)$ and $T_r(dq)$ depend on the crosscoupling. Since $\psi_q(\text{PM}) < 0$, $T_{PM}(q)$ is higher than zero when $\beta < 0^\circ$ and lower than zero when $\beta > 0^\circ$. $T_{PM}(q)$ reaches the peak when $\beta = -50^\circ$, due to $\psi_q(\text{PM})$ being at maximum when $\beta = -30^\circ$ and I_d being at maximum when $\beta = -90^\circ$. $T_r(dq)$ peaks when $\beta = -10^\circ$, since L_{dq} is maximum when $\beta = -30^\circ$ while $I_q^2 - I_d^2$ peaks when $\beta = 0^\circ$.

When $\beta = 0^\circ$, $T_{PM}(q)$ and $T_r(d-q)$ are zero. However, due to the crosscoupling, $T_r(dq)$ and, hence, T_r are less than zero. Therefore, the total torque is lower than the PM torque.

VII. CONCLUSION

The average torque separation based on the Maxwell stress tensor method and the virtual work principle, respectively, have been investigated in this paper when the FP method is employed. It is found that these two methods result in different average torques when the FP method is employed. This discrepancy is due to the influence of equivalent rotational magnetic saliency in the stator, which is a result of interaction of PM and armature fields and causes the improper torque attribution when the Maxwell stress tensor method is used. The average torque components can still be appropriately separated and analyzed by using the virtual work principle when the FP method is employed.

The average torque calculation and separation in association with the FP method can provide valuable insights for the machine design and optimization. The discussions and conclusions are equally applicable to any other type of electrical machines.

APPENDIX

The magnetic energy in the machine is calculated according to the material properties as [14], [15], [38]

$$W_m = \int w_m dV = \int \int_0^B H dB dV. \quad (19)$$

For the nonmagnetic regions, such as air and copper, the magnetic energy density w_m becomes

$$w_{\text{air}} = \frac{B^2}{(2 \mu_0)}. \quad (20)$$

For the soft-magnetic regions, such as iron, the magnetic energy density w_m is calculated as

$$w_{\text{iron}} = \int_0^B H dB. \quad (21)$$

In the hard-magnet regions, w_m is

$$w_{PM} = (B_p - B_r)^2 / 2 \mu_0 \mu_{rp} + B_t^2 / 2 \mu_0 \mu_{rt} \quad (22)$$

where B_r , B_p , and B_t are the remanence, parallel, and tangential flux densities, respectively; and μ_{rp} and μ_{rt} are the relative recoil permeability on parallel and tangential directions.

REFERENCES

- [1] A. M. El-Refai, "Fractional-slot concentrated-windings synchronous permanent magnet machines: Opportunities and challenges," *IEEE Trans. Ind. Electron.*, vol. 57, no. 1, pp. 107–121, Jan. 2010.
- [2] Z. Q. Zhu, "Fractional slot permanent magnet brushless machines and drives for electrical and hybrid propulsion systems," *Int. J. Comput. Math. Electr. Electron. Eng.*, vol. 30, no. 1, pp. 9–31, 2011.

- [3] D. G. Dorrell, M. Hsieh, and A. M. Knight, "Alternative rotor designs for high performance brushless permanent magnet machines for hybrid electric vehicles," *IEEE Trans. Magn.*, vol. 48, no. 2, pp. 835–838, Feb. 2012.
- [4] A. Wang, Y. Jia, and W. L. Soong, "Comparison of five topologies for an interior permanent-magnet machine for a hybrid electric vehicle," *IEEE Trans. Magn.*, vol. 47, no. 10, pp. 3606–3609, Oct. 2011.
- [5] H. Li and Z. Chen, "Overview of different wind generator systems and their comparisons," *IET Renew. Power Generat.*, vol. 2, no. 2, pp. 123–138, 2008.
- [6] E. M. Tsampouris, M. E. Beniakar, and A. G. Kladas, "Geometry optimization of PMSMs comparing full and fractional pitch winding configurations for aerospace actuation applications," *IEEE Trans. Magn.*, vol. 48, no. 2, pp. 943–946, Feb. 2012.
- [7] M. Villani, M. Tursini, G. Fabri, and L. Castellini, "High reliability permanent magnet brushless motor drive for aircraft application," *IEEE Trans. Ind. Electron.*, vol. 59, no. 5, pp. 2073–2081, May 2012.
- [8] W. P. Cao, B. C. Mecrow, G. J. Atkinson, J. W. Bennett, and D. J. Atkinson, "Overview of electric motor technologies used for more electric aircraft (MEA)," *IEEE Trans. Ind. Electron.*, vol. 59, no. 9, pp. 3523–3531, Sep. 2012.
- [9] W. Fei, P. Luk, J. Ma, J. X. Shen, and G. Yang, "A high-performance line-start permanent magnet synchronous motor amended from a small industrial three-phase induction motor," *IEEE Trans. Magn.*, vol. 45, no. 10, pp. 4724–4727, Oct. 2009.
- [10] S. Salon, S. Bhatia, and D. Burow, "Some aspects of torque calculations in electrical machines," *IEEE Trans. Magn.*, vol. 33, no. 2, pt. 2, pp. 2018–2021, Mar. 1997.
- [11] J. Coulomb, "A methodology for the determination of global electromechanical quantities from a finite element analysis and its application to the evaluation of magnetic forces, torques and stiffness," *IEEE Trans. Magn.*, vol. MAG-19, no. 6, pp. 2514–2519, Nov. 1983.
- [12] W. Muller, "Comparison of different methods of force calculation," *IEEE Trans. Magn.*, vol. 26, no. 2, pp. 1058–1061, Mar. 1990.
- [13] M. Marinescu and N. Marinescu, "Numerical computation of torques in permanent magnet motors by Maxwell stresses and energy method," *IEEE Trans. Magn.*, vol. MAG-24, no. 1, pp. 463–466, Jan. 1988.
- [14] D. Howe and Z. Q. Zhu, "The influence of finite element discretisation on the prediction of cogging torque in permanent magnet excited motors," *IEEE Trans. Magn.*, vol. MAG-28, no. 2, pp. 1080–1083, Mar. 1992.
- [15] D. M. Ionel, M. Popescu, M. I. McGilp, T. J. E. Miller, and S. J. Dellinger, "Assessment of torque components in brushless permanent-magnet machines through numerical analysis of the electromagnetic field," *IEEE Trans. Ind. Appl.*, vol. 41, no. 5, pp. 1149–1158, Sep.-Oct. 2005.
- [16] M. Popescu, D. M. Ionel, T. J. E. Miller, S. J. Dellinger, and M. I. McGilp, "Improved finite element computations of torque in brushless permanent magnet motors," *Inst. Electr. Eng. Proc.—Electr. Power Appl.*, vol. 152, no. 2, pp. 271–276, 2005.
- [17] N. Bianchi and L. Alberti, "MMF harmonics effect on the embedded FE analytical computation of PM motors," *IEEE Trans. Ind. Appl.*, vol. 46, no. 2, pp. 812–820, Mar.-Apr. 2010.
- [18] N. A. Demerdash, R. Wang, and R. Secunde, "Three dimensional magnetic fields in extra high speed modified Lundell alternators computed by a combined vector-scalar magnetic potential finite element method," *IEEE Trans. Energy Conv.*, vol. 7, no. 2, pp. 353–366, Jun. 1992.
- [19] G. Qi, J. T. Chen, Z. Q. Zhu, D. Howe, L. B. Zhou, and C. L. Gu, "Influence of skew and cross-coupling on flux-weakening performance of permanent-magnet brushless AC machines," *IEEE Trans. Magn.*, vol. 45, no. 5, pp. 2110–2117, May 2009.
- [20] N. Bianchi and S. Bolognani, "Magnetic models of saturated interior permanent magnet motors based on finite element analysis," in *Proc. IEEE Ind. Appl. Conf.*, 1998, vol. 1, pp. 27–34.
- [21] J. Hu, J. Zou, and W. Liang, "Finite element calculation of the saturation dq-axes inductance for a direct drive PM synchronous motor considering cross-magnetization," in *Proc. 5th Int. Conf. Power Electron. Drive Syst.*, 2003, vol. 1, pp. 677–681.
- [22] J. K. Tangudu, T. M. Jahns, A. M. El-Refai, and Z. Q. Zhu, "Segregation of torque components in fractional-slot concentrated-winding interior PM machines using frozen permeability," in *Proc. IEEE Energy Conv. Congr. Expo.*, pp. 3814–3821.
- [23] S. Williamson and A. M. Knight, "Performance of skewed single-phase line-start permanent magnet motors," *IEEE Trans. Ind. Appl.*, vol. 35, no. 3, pp. 577–582, May/Jun. 1999.
- [24] G. H. Kang, J. P. Hong, G. T. Kim, and J. W. Park, "Improved parameter modeling of interior permanent magnet synchronous motor based on finite element analysis," *IEEE Trans. Magn.*, vol. 36, no. 4, pt. 1, pp. 1867–1870, Jul. 2000.
- [25] J. A. Walker, D. G. Dorrell, and C. Cossar, "Flux-linkage calculation in permanent-magnet motors using the frozen permeabilities method," *IEEE Trans. Magn.*, vol. 41, no. 10, pp. 3946–3948, Oct. 2005.
- [26] S. Y. Kwak, J. K. Kim, and H. K. Jung, "Characteristic analysis of multilayer-buried magnet synchronous motor using fixed permeability method," *IEEE Trans. Energy Conv.*, vol. 20, no. 3, pp. 549–555, Sep. 2005.
- [27] J. A. Walker, D. G. Dorrell, and C. Cossar, "Effect of mutual coupling on torque production in switched reluctance motors," *J. Appl. Phys.*, vol. 99, no. 10, pp. 08R304–08R304-3, 2006.
- [28] K. Shirai, Y. Tokikuni, K. Shima, T. Fukami, R. Hanaoka, and S. Takata, "Causes of increase in the terminal voltage of a permanent-magnet-assisted salient-pole synchronous machine," in *Proc. Int. Conf. Electr. Mach. Syst.*, 2009, DOI: 10.1109/ICEMS.2009.5382931.
- [29] G. Dajaku and D. Gerling, "Magnetic radial force density of the PM machine with 12-teeth/10-poles winding topology," in *Proc. IEEE Int. Electr. Mach. Drives Conf.*, 2009, pp. 1715–1720.
- [30] Z. P. Xia, Z. Q. Zhu, L. J. Wu, and G. W. Jewell, "Comparison of radial vibration forces in 10-pole/12-slot fractional slot surface-mounted and interior PM brushless AC machines," in *Proc. Int. Conf. Electr. Mach.*, Rome, Italy, 2010, DOI: 10.1109/ICELMACH.2010.5608062.
- [31] T. J. E. Miller, M. Popescu, C. Cossar, and M. I. McGilp, "Computation of the voltage-driven flux-MMF diagram for saturated PM brushless motors," in *Rec. Ind. Appl. Conf.*, 2005, vol. 2, pp. 1023–1028.
- [32] Y. Liu, Z. Q. Zhu, and D. Howe, "Direct torque control of brushless DC drives with reduced torque ripple," *IEEE Trans. Ind. Appl.*, vol. 41, no. 2, pp. 599–608, Mar.-Apr. 2005.
- [33] R. H. Park, "Two-reaction theory of synchronous machines generalized method of analysis—Part I," *Trans. Amer. Inst. Electr. Eng.*, vol. 48, no. 3, pp. 716–727, 1929.
- [34] R. H. Park, "Two-reaction theory of synchronous machines—Part II," *Trans. Amer. Inst. Electr. Eng.*, vol. 52, no. 2, pp. 352–354, 1933.
- [35] M. Barcaro, N. Bianchi, and F. Magnussen, "Remarks on torque estimation accuracy in fractional-slot permanent magnet motors," *IEEE Trans. Ind. Electron.*, vol. 59, no. 6, pp. 2565–2572, Jun. 2012.
- [36] F. Meier and J. Soulard, "Dq theory applied to a permanent magnet synchronous machine with concentrated windings," in *Proc. IET Conf. Power Electron. Mach. Drives*, 2008, pp. 194–198.
- [37] A. Zulu, B. Mecrow, and M. Armstrong, "Investigation of the dq-equivalent model for performance prediction of flux-switching synchronous motors with segmented-rotors," *IEEE Trans. Ind. Electron.*, vol. 59, no. 6, pp. 2393–2402, Jun. 2011.
- [38] P. Campbell, "Comments on energy stored in permanent magnets," *IEEE Trans. Magn.*, vol. 36, no. 1, pp. 401–403, Jan. 2000.